Real-time three-dimensional infrared imaging using fringe projection profilometry

Chao Zuo (左 超)[1,2,3*], Qian Chen (陈 钱)[1,3], Shijie Feng (冯世杰)[1], Guohua Gu (顾国华)[1], and Anand Asundi[2]

[1] *Jiangsu Key Laboratory of Spectral Imaging & Intelligence Sense, Nanjing University of Science and Technology, Nanjing 210094, China*

[2] *Centre for Optical and Laser Engineering, School of Mechanical and Aerospace Engineering, Nanyang Technological University, Singapore 639798, Singapore*

[3] *Key Laboratory of Photoelectronic Imaging Technology and System, Ministry of Education of China, Beijing Institute of Technology, Beijing 100081, China*

[*] *Corresponding author: surpasszuo@163.com*

Received January 23, 2013; accepted March 1, 2013; posted online July 30, 2013

Infrared thermography determines the surface temperature of an object or human body. It is a promising imaging technology for medical and biological observations due to its contactless and completely non-invasive properties. However, traditional two-dimensional (2D) infrared thermography cannot retain the spatial information, and thus provides only qualitative diagnosis information. A novel real-time three-dimensional (3D) infrared imaging system which takes full advantages of high-speed, high-quality, high-sensitivity, and low-cost in 3D thermograph is presented. We demonstrate the real-time 3D thermal imaging at the speed of 24 frames per second (fps), with resolution of 640 × 480 points. Experimental results demonstrate quantitatively measurement of temperature distribution of 3D surfaces in real-time is realized with this system.

OCIS codes: 110.0110, 110.3080, 110.6880, 50.6910.
doi: 10.3788/COL201311.S21101.

Infrared thermal imaging as an economical, fast, non-invasive, non-contact imaging technology has been used in medical diagnosis over fifty years[1]. As a typical infrared radiation source, human body enjoys high radiation power with a peak wavelength of the radiation of 9.348 μm. Human body temperature distribution is influenced by many biological and physiological complex factors (e.g. the heat exchange processes between skin tissues, metabolic activity, vasculature, circadian rhythm, and the regulating of the sympathetic and parasympathetic activity for maintaining homeostasis)[2]. Many diseases, such as thyroid disease, pediatric disease, pain syndrome, early breast cancer, would give rise to skin surface temperature distribution anomaly so that can be detected and diagnosed based on infrared thermograms, effectively[3,4].

Despite the evident merits and great improvements, infrared thermal imaging technology has not gained acceptance in the medical and veterinary communities as a necessary or effective tool in inflammation and tumor detection[5]. One important reason for that is traditional infrared imager is only able to provide two-dimensional (2D) thermograms, which cannot retain the spatial information, such as shape, positions, area, size, etc. The dependence on the distance and angle between the camera and the observed object makes it is very difficult to carry out quantitative and reproducible measurements or to correlate two different 2D thermograms of the same object. There is a need for standardizing thermograms in order to solve this problem[6]. Many studies and analyses have dealt with the problem of standardization of thermograms and provide three dimensional (3D) thermograms to allow quantitative detection and diagnose. Integrating 3D shape measurement techniques with thermograms can help creating standardized thermograms[5,6]. However, traditional 3D scanning profilometers are usually designed to measure static object shapes under non-time-critical measurement. It is desirable that the 3D information can be acquired in real-time so that the details of temperature and shape changes in an instant can be captured, which can provide in-depth visual insights into events that happen during detection, diagnose or surgical operations[7].

The goal of this letter is to introduce a novel real-time 3D infrared imaging system which takes full advantages of high-speed, high-quality, high-sensitive, and low-cost in 3D thermograph. More specifically, we combine our recently reported real-time 3D shape measurement technology[8] with 2D thermal images to generate real-time 3D thermograph. We demonstrate the real-time 3D thermal imaging at the speed of 24 frames per second (fps), with resolution of 640 × 480 points. Such a system firstly enables us to measure quantitatively the heat flux emitted from the surface of a subject in real-time and

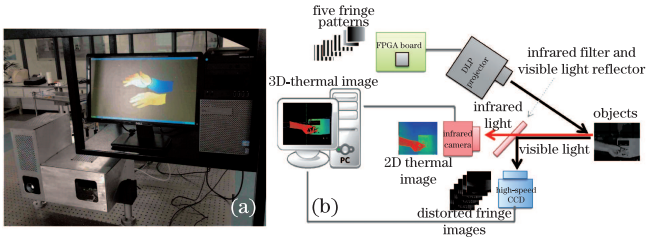

Fig. 1. (a) The real-time 3D thermal imaging system and (b) its schematic diagram.

allows us to quantitatively standardize the thermograph for comparison or statistical analysis.

Figure 1(a) shows a photograph of the real-time 3D infrared imaging system we developed. Figure 1(b) shows its schematic diagram. The present configuration includes an modified off-the-shelf digital light processing (DLP) projector, a high-speed charge-coupled device (CCD) camera (GE680, Allied Vision Technologies, Germany), a self-developed pattern generation field-programmable gate array (FPGA) board, a digital thermal camera FLIR Photon 640 (640×512 VOx Microbolometer) and an infrared/visible light splitter made of coated germanium with about 90% transmittance in mid-to-long infrared waveband and high reflectance in visible waveband. The projector we used is a low-cost, a single-chip DLP projector (X1161PA, Acer). The color wheel of the DLP projector is removed to make the projector operate in a monochrome mode. The FPGA board is designed to generate structure light patterns to the projector and control the timing signals among the projector, the high-speed CCD camera, and the infrared camera. When the fringe patterns are projected on to the objects with high switching rate, they will be distorted and phase information in the distorted fringe patterns can be extracted through phase-shifting algorithm[9]. The phase information can be converted to 3D coordinate through calibration[8,10]. Together with the reflected fringe pattern in the visible band, the infrared light or heat flux emitted from the object surface reached the infrared/visible light filter. They are split and then captured by the infrared camera and the high-speed CCD camera, respectively. Finally, the surface temperature of the target object acquired by the infrared camera is mapped onto the 3D surface of the object to obtain the temperature distribution.

Since the frame rate of the infrared camera is 25 Hz. To match this speed and simplify the intensity calibration procedure of the projector, only the red channel signal is used and the high speed CCD camera was operated at a frame-rate of 120 fps. The red-channel-only patterns were switched at 120 Hz and controlled by the FPGA board. To reconstruct 3D video fast and reliably, we propose a bi-frequency phase-shifting method in which five patterns are used for one 3D reconstruction. The first three sinusoidal structure patterns form a three-step phase-shifting and the fringe images can be described as

$$I_1(x,y) = A(x,y) + B(x,y)\cos(\varphi_1 - 2\pi/3), \quad (1)$$

$$I_2(x,y) = A(x,y) + B(x,y)\cos(\varphi_1), \quad (2)$$

$$I_3(x,y) = A(x,y) + B(x,y)\cos(\varphi_1 + 2\pi/3), \quad (3)$$

where (x,y) is the camera coordinate, $A(x,y)$ is the average intensity relating to the pattern brightness and background illumination, $B(x,y)$ is the intensity modulation relating to the pattern contrast and surface reflectivity. φ_1 is the corresponding wrapped phase map which can be extracted by

$$\phi_1(x,y) = \tan^{-1} (\sqrt{3}(I_1 - I_3)/(2I_2 - I_1 - I_3). \quad (4)$$

Since the arctangent function only ranges from $-\pi$ to π, the phase value provided from Eq. (4) has π phase discontinuities. To obtain an absolute phase distribution, a phase unwrapping algorithm is usually needed. The absolute phase distribution is necessary for 3D shape measurement of isolated objects with complex shapes. Spatial phase unwrapping algorithms cannot resolve the phase ambiguity in discontinuous surfaces and large step height changes where the phase changes large than π[11]. In order to obtain the reliable absolute phase distribution of a deformed fringe pattern, another two fringe images with π phase-shift are used as

$$I_4(x,y) = A(x,y) + B(x,y)\sin(\varphi_2), \quad (5)$$

$$I_5(x,y) = A(x,y) + B(x,y)\cos(\varphi_2). \quad (6)$$

Assuming that both the CCD camera and the projector have a fairly large depth-of-view and the reflection of the object surface is linear, the average intensity coefficients $A(x,y)$ should be constant for pixel (x,y) in all the five images. It can be calculated using

$$A(x,y) = (I_1(x,y) + I_2(x,y) + I_3(x,y))/3. \quad (7)$$

Utilizing the $A(x,y)$ obtained, another wrapped phase map φ_2 can be computed as

$$\varphi_2(x,y) = \tan^{-1}\Big((I_4 - A)/(I_5 - A)\Big). \quad (8)$$

By now we have obtained two wrapped phase maps: φ_1 and φ_2 by using only five fringe patterns. Note φ_2 is different from φ_1 when the fringe frequency of I_4 and I_5 is not equal to that of $I_1 \sim I_3$, which is exactly what we wanted because they provided extra information to carry out the phase unwrapping, so that the absolute phase map for isolated objects or object containing sharp height variations can be recovered. Retrieving the absolute phase maps Φ_1 or Φ_2 from the wrapped ones, φ_1 and φ_2, we have

$$\begin{cases} \Phi_1(x,y) = \varphi_1(x,y) + 2\pi k_1(x,y) \\ \Phi_2(x,y) = \varphi_2(x,y) + 2\pi k_2(x,y) \end{cases}. \quad (9)$$

And they should have the following relationship:

$$\Phi_1(x,y) = (\lambda_2/\lambda_1)\,\Phi_2(x,y), \quad (10)$$

where λ_1 and λ_2 are the wavelengths for one fringe period, $k_1(x,y)$ and $k_2(x,y)$ are fringe orders. To eliminate ambiguity in assignment of unwrapped fringe order, a straightforward method is to obtain a low-resolution phase with a set of unit frequency patterns (λ_2 is large enough to cover the view of the camera) so that the calculated phase (e.g., $\varphi_2(x,y)$) has a range of less than 2π[12]. In this case, no phase unwrapping is required for $\varphi_2(x,y)$, i.e., $\Phi_2(x,y) = \varphi_2(x,y)$. Combining Eqs. (9) and (10), we can obtain $k_1(x,y)$ for each pixel easily. By this means the phase $\varphi_1(x,y)$ at higher spatial frequency can be successfully unwrapped. Since fine fringes are needed for one 3D reconstruction, the imaging speed of our system is 24 fps which matched the speed of the thermal camera very well. The speed can be further increased if a higher-frame-rate thermal camera is employed.

The designed system should be carefully calibrated before used. Firstly, nonuniformity correction and temperature calibration should be performed to reduce the spatial noise and establish the relationship between the grayscale

with the temperature. By utilizing a standard blackbody irradiation source, the nonlinearity response of the thermal camera is calibrated through multi-point nonuniformity correction[13]. Besides, scene-based nonuniformity corrections[14−16] can also be applied to compensate the temporal offset drifts of the detector responses. But it will compromise the radiometric accuracy of the temperature measurement.

To determine the 3D coordinate of each point of the object, system calibration should be performed. Once the system calibration is done, the parameter matrix of the CCD camera ($\mathrm{P_c}$) and the projector ($\mathrm{P_p}$) can be obtained based on the calibrated intrinsic and extrinsic parameters of the camera ($\mathrm{A_c}$ and $\mathrm{M_c}$) and the projector ($\mathrm{A_p}$) and ($\mathrm{M_p}$):

$$\mathrm{P_c} = \mathrm{A_c M_c} = \begin{pmatrix} p_{11}^{\mathrm{c}} & p_{12}^{\mathrm{c}} & p_{13}^{\mathrm{c}} & p_{14}^{\mathrm{c}} \\ p_{21}^{\mathrm{c}} & p_{22}^{\mathrm{c}} & p_{23}^{\mathrm{c}} & p_{24}^{\mathrm{c}} \\ p_{31}^{\mathrm{c}} & p_{32}^{\mathrm{c}} & p_{33}^{\mathrm{c}} & p_{34}^{\mathrm{c}} \end{pmatrix}, \tag{11}$$

and

$$\mathrm{P_p} = \mathrm{A_p M_p} = \begin{pmatrix} p_{11}^{\mathrm{p}} & p_{12}^{\mathrm{p}} & p_{13}^{\mathrm{p}} & p_{14}^{\mathrm{p}} \\ p_{21}^{\mathrm{p}} & p_{22}^{\mathrm{p}} & p_{23}^{\mathrm{p}} & p_{24}^{\mathrm{p}} \\ p_{31}^{\mathrm{p}} & p_{32}^{\mathrm{p}} & p_{33}^{\mathrm{p}} & p_{34}^{\mathrm{p}} \end{pmatrix}. \tag{12}$$

The relationship between the CCD camera coordinates and the projector coordinates can then be established via the absolute phase for each arbitrary coordinate (x, y) on the camera plane. The absolute phase $\Phi_1(x, y)$ can be easily converted to the projector coordinate x^p. Finally, the world coordinate $(x^{\mathrm{w}}, y^{\mathrm{w}}, z^{\mathrm{w}})$ is given by

$$\begin{pmatrix} x^{\mathrm{w}} \\ y^{\mathrm{w}} \\ z^{\mathrm{w}} \end{pmatrix} = \begin{pmatrix} p_{11}^{\mathrm{c}} - p_{31}^{\mathrm{c}} x & p_{12}^{\mathrm{c}} - p_{32}^{\mathrm{c}} x & p_{13}^{\mathrm{c}} - p_{33}^{\mathrm{c}} x \\ p_{21}^{\mathrm{c}} - p_{31}^{\mathrm{c}} y & p_{22}^{\mathrm{c}} - p_{32}^{\mathrm{c}} y & p_{23}^{\mathrm{c}} - p_{33}^{\mathrm{c}} y \\ p_{11}^{\mathrm{p}} - p_{31}^{\mathrm{p}} x^{\mathrm{p}} & p_{12}^{\mathrm{c}} - p_{31}^{\mathrm{p}} x^{\mathrm{p}} & p_{13}^{\mathrm{p}} - p_{33}^{\mathrm{p}} x^{\mathrm{p}} \end{pmatrix}^{-1} \begin{pmatrix} p_{34}^{\mathrm{c}} x - p_{14}^{\mathrm{c}} \\ p_{34}^{\mathrm{c}} y - p_{24}^{\mathrm{c}} \\ p_{34}^{\mathrm{p}} x^{\mathrm{p}} - p_{14}^{\mathrm{p}} \end{pmatrix}. \tag{13}$$

To map the 2D thermal image to the 3D point cloud obtained, it is necessary to perform coordinate transformation in order to match the pixels of the two cameras. For this purpose, projective transformation is preformed and the transformation matrix were determined once through calibration. To compute intrinsic and extrinsic parameters of the thermal camera, a black and white checkerboard panel is used. The panel is heated just before calibration, so the infrared camera is able to detect the calibration pattern due to that black and white colored objects have very different emissivity factors. This means that a black object emits more thermal radiation than a white object if both are illuminated using white light, even though the both objects are at the same temperature. Once the coordinate relationship between the two cameras is determined, we can identify the corresponding pixel of any 3D image pixel in the 2D thermal image for mapping propose.

We examined the performance of our system by measuring a complex scene which consists of two spatially isolated objects - a stationary power box and a moving hand. Figure 2 displays one snapshot of the measurement result. The five fringe images captured by the high-speed CCD are shown in Figs. 2(a)–(e), from which the absolute phase map can be obtained and the 3D coordinates of the objects can be reconstructed by the system calibration parameters. Meanwhile, the 2D thermal image which is properly aligned with the CCD image is shown in absolute temperature coded pseudo-color (Fig. 2(f)). The final reconstructed 3D thermal images obtained by mapping the thermal images to the 3D geometry are displayed in Figs. 2(g)–(j) from different viewpoints. The world coordinates $(x^{\mathrm{w}}, y^{\mathrm{w}}, y^{\mathrm{w}})$ were labeled as red, green, and blue lines, respectively. These results prove that our system can accurately obtain the 3D shape and effectively acquire the temperature distribution on the surface of the target objects.

To verify the real-time measurement performance of our system, a 3D infrared video sequence was recorded and several frames were extracted, displayed in Fig. 3. It can be seen that 3D shapes of the hand could be well reconstructed despite it was in continuous motion. Besides, the remaining heat on the surface of the power box is accurately captured by our system with both temperature distribution and the 3D coordinate information.

In conclusion, a high-resolution, real-time 3D infrared imaging system is developed. The 3D shape acquisition speed can be up to 24 fps for the current setup. The speed can be further increased if a thermal camera with a higher frame rate is employed. A bi-frequency phase-shifting algorithm is proposed for fast 3D shape reconstruction. It employs only five projection fringes to

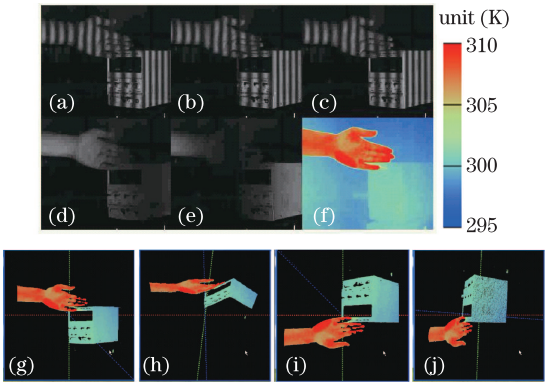

Fig. 2. (Color online) 3D thermograms reconstruction result. (a–e) Five images of tested objects with deformed fringe patterns captured by the CCD; (f) 2D thermal image; (g–j) reconstructed 3D thermograms viewed from different angles.

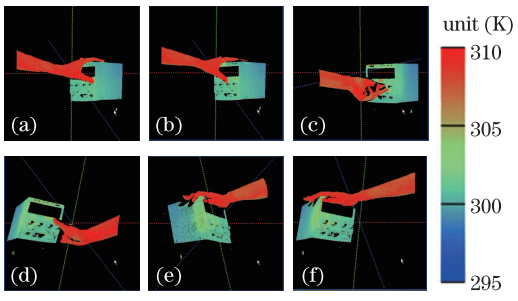

Fig. 3. (Color online) Real-time 3D thermal imaging results of a moving hand and a stationary power box.

realize full-field phase unwrapping in the presence of discontinuous or isolated objects. By properly calibrating the infrared camera and the 3D fringe projection system, the absolute phase can be converted to 3D coordinate and the 2D thermal image can be mapped to the 3D surface to obtain the 3D thermogram. 3D thermogram is a spatial model of observed object that contains surface shape and temperature distribution data. Thus it can be a valuable data model for current and future applications for modeling and simulating biological and physiological processes of the human body. Furthermore, the real-time nature of our system will bring novel opportunities for different medical applications, such as noninvasive medical diagnosis and surgical operations.

This work was supported by the Research Fund for the Doctoral Program of Ministry of Education of China (No. 20123219110016) and the National Natural Science Foundation of China (No. 61271332), and the Research and Innovation Plan for Graduate Students of Jiangsu Higher Education Institutions, China (No. CXZZ11_0237). Chao Zuo gratefully acknowledges the financial support from China Scholarship Council (No. 201206840009).

References

1. B. Kateb, V. Yamamoto, C. Yu, W. Grundfest, and J. P. Gruen, Neuroimage **47,** T154 (2009).
2. H. H. Pennes, J. Appl. Physiol. **1,** 93 (1948).
3. N. Isogai and H. Kamiishi, Head & Neck **19,** 143 (1997).
4. G. Schaefer, M. Závišk, and T. Nakashima, Pattern Recogn. **42,** 1133 (2009).
5. X. Ju, J.-C. Nebel, and J. P. Siebert, Proc. SPIE **5640,** 266 (2005).
6. I. Grubisic, L. Gjenero, T. Lipic, I. Sovic, and T. Skala, in *Proceedings of MIPRO, 2011 Proceedings of the 34th International Convention* 269 (2011).
7. Y. Okada, T. Kawamata, A. Kawashima, and T. Hori, Neurosurgery **60,** 362 (2007).
8. C. Zuo, Q. Chen, G. Gu, S. Feng, and F. Feng, Opt. Express **20,** 19493 (2012).
9. C. Zuo, Q. Chen, S. J. Feng, F. Feng, G. H. Gu, and X. B. Sui, Appl. Opt. **51,** 4477 (2012).
10. S. Zhang and P. S. Huang, Opt. Eng. **45,** 083601 (2006).
11. T. R. Judge and P. J. Bryanston-Cross, Opt. Laser. Eng. **21,** 199 (1994).
12. J. G. Zhong and Y. L. Zhang, Appl. Opt. **40,** 492 (2001).
13. M. Schulz and L. Caldwell, Infrared Phys. Technol. **36,** 763 (1995).
14. C. Zuo, Q. Chen, G. H. Gu, and X. B. Sui, J. Opt. Soc. Am. A: Opt. Image Sci. Vis. **28,** 1164 (2011).
15. C. Zuo, Q. A. Chen, G. H. Gu, and W. X. Qian, Opt. Rev. **18,** 197 (2011).
16. C. Zuo, Q. Chen, G. H. Gu, X. B. Sui, and J. L. Ren, Infrared Phys. Technol. **55,** 263 (2012).